Materials Advances

ROYAL SOCIETY OF CHEMISTRY

PAPER

View Article Online
View Journal | View Issue

Cite this: *Mater. Adv.*, 2022, 3, 9103

Magnetic–dielectric bistabilities and magnetodielectric coupling effects in a new layered hybrid perovskite: $(C_6H_5(CH_2)_4NH_3)_2[MnCl_4]$†

Bo Huang,[ab] Ping Wang,[b] Wei-Xiong Zhang *[a] and Xiao-Ming Chen[a]

Received 10th October 2022,
Accepted 28th October 2022

DOI: 10.1039/d2ma00963c

rsc.li/materials-advances

Bistabilities and coupling effects of multiple physical channels in molecule-based materials have attracted widespread interest in the field of sensors, switches, and memory devices. Seeking such materials and understanding the relationship between the changeable physical properties and crystal structures are of great importance for promoting their applications in next-generation devices. Herein, we report a new organic–inorganic layered hybrid perovskite, $(C_6H_5(CH_2)_4NH_3)_2[MnCl_4]$, which undergoes three reversible structural phase transitions in the temperature range of 100–380 K. Crystal analyses indicated that the gradual freezing of the organic cations and tilting of the $MnCl_6$ octahedra, together with the stagger movement of the inorganic layers, induce remarkable thermal-induced magnetic and dielectric bistabilities. Magnetization measurements revealed that the title compound is a canted antiferromagnet below 37 K and shows a spin-flop transition at ±1.4 T at 3 K. Benefiting from the relatively strong interactions between the magnetic layer and crystal lattice, an intrinsic magnetodielectric coupling effect around the spin-flop transition was observed at 3 K. These findings throw light on the further design of advanced magnetodielectric materials based on diverse layered perovskites.

Introduction

Bistable molecule-based materials exhibiting two stable states controllable by external stimuli such as heat, pressure, light, electric, and magnetic field have recently received intense interest owing to their potential applications in sensors, displays, switches, and memory devices.[1] Outstanding examples are crystalline materials with interesting dynamic behaviors such as spin transition, change transfer, proton transfer, molecular reorientation, and structural phase transition.[2–7] Recent decades have witnessed the emergence of numerous molecule-based materials revealing bistabilities in multiple physical channels, such as the bistabilities in dielectric, piezoelectric, and nonlinear-optic properties in ferroelectrics, bistable conductivity in proton-transfer conductors, and the bistable magnetic properties in charge-transfer magnets.[8–10] Smart devices with multi-bistability would be more attractive in the advancement of information technology, for their high capacity of information storage and multiple physical channels to control and receive signals.[11] To obtain multi-bistable molecule-based materials, one effective way is designing two or more functional components in a single-phase material, using switchable crystalline states established by dynamic building blocks to control the physical properties. In this regard, organic–inorganic hybrid crystals are excellent candidates thanks to their abundant structural phase transitions accompanied by intriguing properties such as mechanical, optical, electric, magnetic, and multiferroic.[12] The dielectric and magnetic properties were well studied in formate-bridged coordination polymers with a three-dimensional perovskite structure.[13–16] However, owing to the fact that their organic cations have little influence on the rigid frameworks during the structural phase transition, it is hard to find magnetic bistability in such systems. Another series of coordination polymers with azido-bridged frameworks shows remarkable magnetic bistability, benefiting from the relatively flexible coordination susceptible to the dynamic change of organic cations, but without noticeable dielectric bistability.[17] In contrast, some materials with lower-dimensional coordination

[a] *MOE Key Laboratory of Bioinorganic and Synthetic Chemistry, School of Chemistry, Sun Yat-Sen University, Guangzhou, 510275, P. R. China. E-mail: zhangwx6@mail.sysu.edu.cn*
[b] *Faculty of Chemistry and Chemical Engineering, Yunnan Normal University, Kunming, 650500, P. R. China*

† Electronic supplementary information (ESI) available: Photo of a crystal, powder X-ray diffraction patterns, thermogravimetric curve, two heating–cooling circles of DSC curves, inorganic layers, summary of crystal data and structural refinements, selected bond lengths, selected angles, and geometry of hydrogen bonds. CCDC 2095542 (120 K), 2095544 (293 K), 2095547 (345 K) and 2095550 (373 K). For ESI and crystallographic data in CIF or other electronic format see DOI: https://doi.org/10.1039/d2ma00963c

layers, chains, or discrete units were found to be more susceptible to structural phase transitions to yield multi-switchable properties.[18–21] In this respect, to acquire multi-bistable molecule-based materials, a relatively flexible crystal structure with strong interactions between organic and inorganic components is crucial.

Besides thermo-sensitive bistability, field-controlled switchable physical properties, such as the magnetodielectric effect (a typical magnetoelectric effect), have invoked significant research activities as well, for the goal of realizing potential applications in energy transformation devices and information storage systems.[22–25] In recent decades, the magnetodielectric effect has been widely investigated in oxide materials, and plenty of excellent fundamental research and technologies have been achieved.[26–28] For example, the large magnetodielectric effect in $DyMnO_3$,[29] $TbMnO_3$,[30] and $TbMn_2O_5$,[31] the room-temperature magnetodielectric response in $LuFe_2O_4$,[32] and the low-field magnetodielectric effect in $Sr_3Co_2Fe_{24}O_{41}$.[33] Simultaneously, tremendous progress has been made in organic–inorganic hybrid crystals,[34–46] such as the giant and room-temperature coupling effect in metal-formate frameworks and highly reproducible coupling effect in layered perovskites.[47,48] Seeking new multiferroic materials with robust magnetoelectric coupling effect is still a desirable purpose in this field. The studies on the relationship between dielectric and magnetic properties based on microscopic crystal structures are of great importance in the rational design of such multiferroic materials.

In our previous studies on layered hybrid perovskite crystals, we found thermal-induced dielectric and magnetic bistabilities during the ferroelastic and ferroelectric phase transitions in ferromagnetics $(C_6H_5(CH_2)_4NH_3)_2[CuCl_4]$,[49] and field-induced magnetodielectric coupling effects in $(C_6H_5CH_2CH_2NH_3)_2[CuCl_4]$ and $(C_6H_5CH_2CH_2NH_3)_2[MnCl_4]$.[48] Compared to three-dimensional metal–organic coordination frameworks, one-dimensional chains and other discrete hybrids, such two-dimensional layered perovskites take advantage of the structural flexibility, strong magnetic exchange interactions and robust hydrogen bonds.[50–58] Herein, as a sequel investigation on thermo-sensitive and field-controllable magnetoelectric materials based on layered perovskites, we synthesized large single-crystal samples of a new layered perovskite, $(C_6H_5(CH_2)_4NH_3)_2[MnCl_4]$ (**1**), and comprehensively investigated its dielectric and magnetic properties by various methods such as differential scanning calorimetry, variable-temperature single-crystal structural analyses, and dielectric, magnetic, and combined magneto-dielectric measurements. We found that **1** undergoes three reversible structural phase transitions in the temperature range of 100–380 K, two of which show remarkable dielectric and magnetic dual-bistabilities, arising from the gradual ordering and displacement of the organic cations, synchronous tilting of the $MnCl_6$ octahedra, and stagger movement of the inorganic layers. Due to the strong interactions between the magnetic layer and crystal lattice, an intrinsic magnetodielectric effect appears during the field-induced spin-flop transition at 3 K. Moreover, compared with its analogue $(C_6H_5CH_2CH_2NH_3)_2[MnCl_4]$, **1** reveals a reduced spin-flop field of $\pm$1.4 T benefiting from its more flexible organic cation.

Experimental section

Synthesis

All chemicals were obtained from commercial sources and used without further purification. The crystal samples suitable for single-crystal X-ray diffraction measurement were obtained by mixing stoichiometric quantities of manganese dichloride (2.5 mmol) and 4-phenylbutylammonium chloride (5 mmol) in a methanol solution (15 mL). Slow evaporation of the clear solution at room temperature over about one week, resulted in light pink flake-shaped crystals of **1** in about 86% yield based on Mn. To obtain large single crystals for the measurement of the magnetodielectric effect, we increased the quantities of raw materials (40 mmol manganese chloride and 80 mmol 4-phenylbutylammonium chloride) and used a mixed solvent of methanol and water (V/V = 1 : 1). After slow evaporation of the clear solution at room temperature for about one month, high-quality crystals with sizes as large as $8.0 \times 4.0 \times 0.3$ mm^3 were obtained (Fig. S1, ESI†). Powder X-Ray diffraction patterns (Cu Kα, λ = 1.54056 Å) were collected on a D8 DA VANCI θ–2θ diffractometer. The experimental powder X-ray diffraction pattern at room temperature matches well with the simulated one (293 K), indicating the purity of the sample (Fig. S2, ESI†). Elemental (C, H, and N) analyses were performed on a PerkinElmer Vario EL elemental analyzer. Elemental analysis (%) for $C_{20}H_{32}N_2MnCl_4$ (497.22) calcd: C, 48.31%; H, 6.49%; N, 5.63%. Found: C, 48.17%, H: 6.10%, N: 5.51%.

Thermal measurements

Thermogravimetric analysis was carried out on a TA Q50 system at a heating rate of 5 K min^{-1} under a N_2 atmosphere from room temperature to 950 K. Differential scanning calorimetry measurements were performed on a TA DSC Q2000 instrument, by heating and cooling the powder sample (6.7 mg) at a rate of 5 K min^{-1} under a N_2 atmosphere in the range of 100–380 K.

Single-crystal X-ray diffraction

Variable-temperature single-crystal X-ray data were collected on a RAXIS IP diffractometer with Mo Kα radiation (λ = 0.71073 Å) at 120, 293, 345, and 373 K, respectively. The structures were solved by direct methods and refined by a least-squares technique based on F^2 with the SHELX software package. All non-H atoms were refined anisotropically using all reflections with $I > 2\sigma(I)$. The hydrogen atoms were generated by geometrical considerations and constrained to their idealized positions. Details of the crystal parameters and structural refinements, selected bond lengths, bond angles and geometry of hydrogen bonds at 120, 293, 345, and 373 K are given in Tables S1–S4 (ESI†), respectively.

Dielectric, magnetic, and magnetodielectric measurements

The temperature dependence of the dielectric constant (ε') was determined using a Tonghui TH2828A LCR meter for the powder-pressed sample at a heating–cooling rate of 2 K min^{-1}. The magnetic properties were determined on a Quantum Design MPMS XL-7 SQUID system with polycrystalline samples.

The magnetodielectric coupling effect was measured by using a combination of a Tonghui TH2828A LCR meter and a Quantum Design physical property measurement system through a modified multifunctional probe with a single crystal sample.

Results and discussion

Thermal properties

Thermogravimetric analysis revealed that **1** is stable up to about 485 K under a N_2 atmosphere (Fig. S3, ESI†). The differential scanning calorimetry (DSC) measurement clearly showed three pairs of thermal anomalies in the range of 100–380 K, indicating three reversible structural phase transitions (Fig. 1). In the heating run, endothermic peaks appear at about 184 K, 338 K, and 354 K, corresponding to exothermic peaks at about 134 K, 335 K, and 352 K in the cooling run, respectively. For convenience, we label the phases below 134/184 K as the α phase, between 134/184 K and 335/338 K as the β phase, between 335/338 K and 352/354 K as the γ phase, and above 352/354 K as the δ phase. Notably, compared with the γ ↔ δ and β ↔ γ phase transitions with very small thermal hysteresis of 2 and 3 K, respectively, the α ↔ β phase transition exhibits an exceptionally large thermal hysteresis of about 50 K. The reproducibility of these structural phase transitions was further confirmed by the second heating–cooling circles of the DSC measurements (Fig. S4, ESI†).

Crystal structure descriptions

Variable-temperature X-ray diffraction measurements revealed that **1** crystallizes in $P2_1/a$ (nonstandard setting of prototypical $P2_1/c$ for convenience of structural comparison) at 120 K (α phase), $P2_1/a$ at 293 K (β phase), *Bmmm* at 345 K (γ phase), and *P*4/*mmm* at 373 K (δ phase), respectively (Table S1, ESI†). It is worth noting that a structure with the same chemical components of **1** was deposited in CSD in 1977,[59] but it belongs to the space group *Cmca* (a = 7.350 Å, b = 47.340 Å, c = 7.380 Å, V = 2567 Å^3) differing from any one of the present four phases of **1**. Structural analyses indicated that **1** belongs to the layered perovskite family with a general formula of A_2MX_4 (the valence ratio of the cation A, metal ion M, and anionic X components are 1, 2, and 1, respectively). As shown in Fig. 2, the structure consists of two-dimensional infinite $[MnCl_4]_n^{2n-}$ inorganic layers made up by corner-sharing $MnCl_6$ octahedra, and these inorganic layers are separated by bilayers of $C_6H_5(CH_2)_4NH_3^+$ cations. These organic bilayers are assembled by weak van der Waals forces and without π···π stacking interaction, giving a flexible character for the entire layered perovskite structure. Every four neighboring $MnCl_6$ octahedra enclose an intralayer cavity, which is occupied by a pair of ammonium ($-NH_3^+$) groups of $C_6H_5(CH_2)_4NH_3^+$ cations from up and down sides. Several N–H···Cl hydrogen bonds are formed between the organic cations and $MnCl_6$ octahedra to provide important medium ways for organic and inorganic layers.

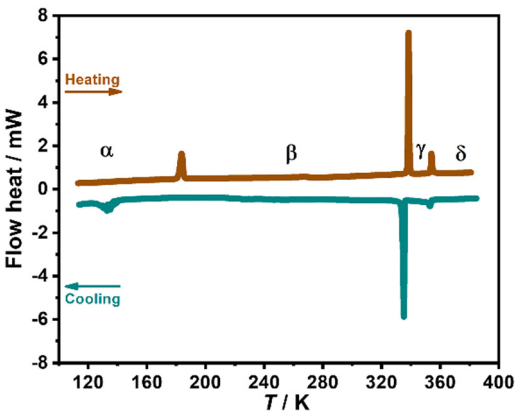

Fig. 1 DSC curves for **1** in a heating–cooling circle.

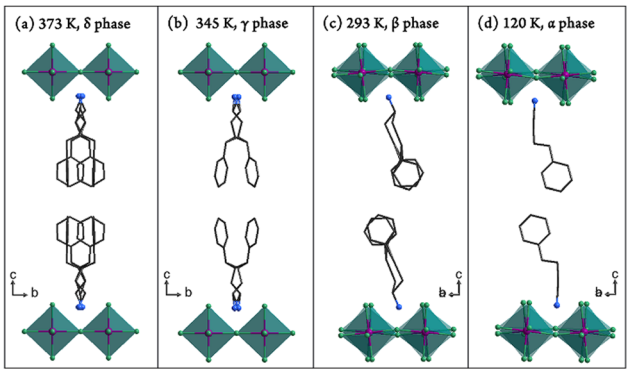

Fig. 2 Crystal structures of **1** at 373 K (a), 345 K (b), 293 K (c), and 120 K (d). Mn, Cl, N, and C atoms are shaded in violet, green, blue, and black, respectively. The organic cations exhibit 8-fold, 4-fold, and 2-fold disorder at 373 K, 345 K, and 293 K, respectively. The H atoms are omitted for clarity.

In the δ phase (373 K), the organic cations are heavily disordered (in 8-fold disorder) and located at the center of the square cavities (Fig. 2(a) and 3(a)). Four longer Mn–Cl2 bonds (2.6023(2) Å) are lying in the layer and two shorter axial Mn–Cl1 bonds (2.457(4) Å) complete a compressed $MnCl_6$ octahedron (Table S2, ESI†). When cooling down to the γ phase (345 K), the cations become 4-fold disordered and are located at the center of the rectangle cavities (Fig. 2(b) and 3(b)). Accordingly, the Mn–Cl bonds lying in the layer are divided into two different types (Mn–Cl2 and Mn–Cl3), resulting in two different distances of neighboring Mn···Mn atoms (5.1706 and 5.1534 Å). However, the angles of Mn–Cl–Mn (in the layer) and Cl–Mn–Cl (perpendicular to the layer) maintain 180°, indicating no sign of tilting for the adjacent $MnCl_6$ octahedra (Table S3, ESI†).

Upon cooling to the β phase (293 K), as shown in Fig. 2(c), the cations become much more ordered (in 2-fold disorder). Their N atoms from up and down sides of the inorganic layer begin to deviate from the vertical axis of the intralayer cavities, indicating the displacement of the organic cations (marked as two red arrows in Fig. 3(c)). Simultaneously, the adjacent $MnCl_6$ octahedra exhibit a slight tilting (blue and orange arrows in Fig. 3(c)), leading to a bent magnetic exchange pathway of Mn–Cl–Mn (167.31(3)°).

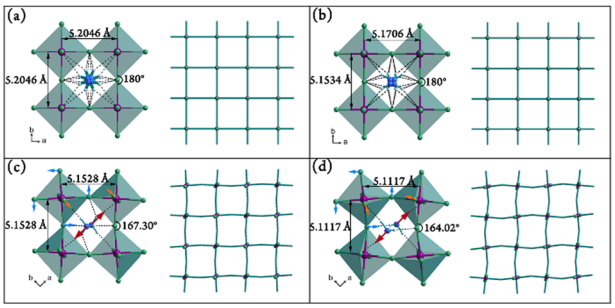

Fig. 3 The $MnCl_6$ octahedra and inorganic layer of **1** at 373 K (a), 345 K (b), 293 K (c), and 120 K (d). Mn, Cl, N, and H atoms are shaded in violet, green, blue, and pale blue, respectively. The C atoms are omitted for clarity. The black dotted lines represent hydrogen bonds. The black double-headed arrows represent the distance between two neighboring Mn···Mn atoms. The blue and orange arrows represent the directions of rotation and tilting of the $MnCl_6$ octahedra, respectively.

With further cooling to the α phase (120 K), the cations become completely frozen (Fig. 2(d)). Compared with those in the β phase, their N atoms deviate much further away from the vertical axis of the intralayer cavities (marked as two red arrows in Fig. 3(d)), indicating a more significant displacement for the organic cations. Meanwhile, the $MnCl_6$ octahedra experience a more drastic tilting (blue and orange arrows in Fig. 3(d)), giving rise to a smaller Mn–Cl–Mn angle (164.02°). In addition, different from the antiparallel (180°) tilting of the neighboring $MnCl_6$ octahedra in the β phase, the angle between the tilting directions in the α phase reduces to 124° (orange arrows in Fig. 3(c) and (d)), indicating a drastic structural transition between β and α phases.

From the δ to α phase, the neighboring inorganic layers along the *c* axis encounter a stagger movement. As shown in Fig. 2(a)–(d), reference to the upper layer, the $MnCl_6$ octahedra of the lower layer are aligned to the upper one in both δ and γ phases, but move to the right side along the *b* axis, hence give the monoclinic unit cells in both β and α phases (Fig. S5, ESI†). Obviously, the interlayer movement in the α phase is much greater than that in the β phase. This stagger arrangement of the inorganic layers may have a considerable influence on the magnetic properties at low temperature (*vide infra*). Besides, the inorganic layer itself changes from a flat fashion (in δ and γ) to a wavy one (in β and α), which may induce a significant change of the energy, and exhibit large endothermic and endothermic peaks during the γ ↔ β transition in the DSC measurement. As shown in the right side of Fig. 3(a)–(d), the magnetic exchange pathways are linear in the δ and γ phases, but become bent in the β and α phases, implying large differences in the magnetic properties of the γ, β, and α phases. In addition, the number of stronger N–H···Cl hydrogen bonds in each intralayer cavity is indistinguishable in both δ and γ phases, and can be clearly distinguished into four and three in the β and α phases, respectively (Table S4, ESI†). Interestingly, the N···Cl distances of the hydrogen bonds are gradually decreased from the δ to α phase, signifying stronger hydrogen bonds at lower temperature. On account of the large displacement of organic cations, drastic tilting of $MnCl_6$ octahedra, and a synchronous notable stagger movement of inorganic layers, the energy barrier of the β ↔ α transition seems to be much larger than the thermal motion at such low temperatures, and thus causes an exceptional large thermal hysteresis of 50 K.

Magnetic properties

The temperature-dependent susceptibility of a polycrystalline sample in 2–300 K under an applied field of 1000 Oe is shown in Fig. 4. The $\chi_M T$ decreases gradually from the room-temperature value of 3.316 $cm^3\ mol^{-1}$ K (lower than the spin-only value of 4.375 $cm^3\ mol^{-1}$ K for Mn^{2+} of $S = 5/2$), to a minimum (0.737 $cm^3\ mol^{-1}$ K) at about 42 K, then slightly increases to a small hump at about 34 K with a further decrease to 0.050 $cm^3\ mol^{-1}$ K at 2 K. For the χ_M, it increases gradually from 0.011 $cm^3\ mol^{-1}$ at 300 K and reaches a broad maximum (0.020 $cm^3\ mol^{-1}$) at 75 K, well indicating the intra-layer antiferromagnetic interactions between Mn^{2+} ions. Then it decreases to a minimum (0.018 $cm^3\ mol^{-1}$) at 42 K followed by a steep rise at lower temperature, suggesting the presence of spontaneous magnetization due to the magnetic long-range ordering arising from spin canting. Fitting the data to above 100 K with the Curie–Weiss law gives a Curie constant of 5.03 $cm^3\ mol^{-1}$ K and a negative Weiss parameter ($\theta = -153.9$ K), indicating strong intralayer antiferromagnetic exchange interactions between the adjacent Mn^{2+} ions. The temperature dependence of the ac magnetic susceptibilities with frequencies of 199 and 997 Hz were measured from 2 to 80 K (Fig. 5). The χ_M' and χ_M'' show no frequency-dependent behavior and exhibit a sharp peak at 37 K, further confirming the long-range magnetic ordering state below 37 K.

Magnetic–dielectric bistabilities

In consideration of the synchronous changes in organic cations and inorganic layers during the phase transitions, we focus on the magnetic and dielectric properties in the vicinity of the structural phase transitions. During the γ ↔ δ transition, as shown in Fig. 6(a), the values of ε' are almost frequency independent. In the heating run, ε' (1000 kHz) is maintained at around 5.40 in the γ phase, then a small but sudden increase

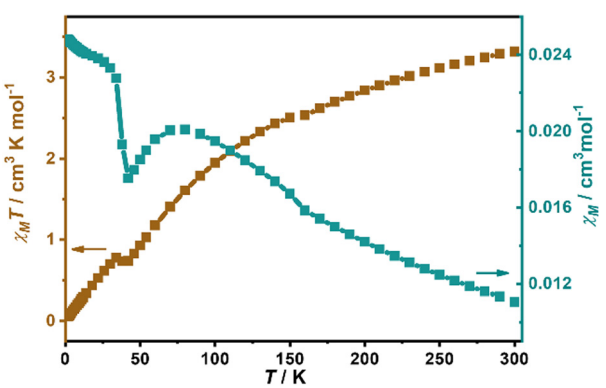

Fig. 4 Temperature dependences of $\chi_M T$ (brown) and χ_M (teal) for a polycrystalline sample of **1** under 1000 Oe.

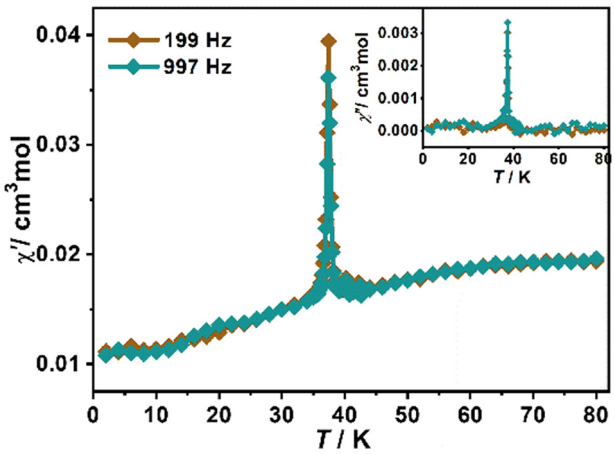

Fig. 5 Temperature dependences of ac magnetic susceptibility in various frequencies for a polycrystalline sample of **1**.

to 5.42 (at 355 K) appears, corresponding to the γ → δ phase transition (the black dotted circle in Fig. 6(a)). After that, ε′ increases slowly to 5.43 (at 366 K). As for the magnetic properties (Fig. 6(b)), there is no obvious anomaly in the temperature dependence of $\chi_M T$ values occurring during the γ ↔ δ transition. From the structural analyses, the small sudden increase of ε′ should be ascribed to the change of molecular dynamics of organic cations from the four-fold to eight-fold disordered states. On the other hand, as the $MnCl_6$ octahedra do not show obvious rotation or tilting during the γ ↔ δ transition, the small change in distance between two neighboring Mn···Mn atoms do not give a noticeable change in the $\chi_M T$ value.

In contrast, during the β ↔ γ transition, ε′ increases slowly from 4.92 (at 303 K, 1000 kHz) to 5.06 (at 336 K), then experiences a step-like increase to 5.40 (at 340 K) in a heating run, and a reverse step-like drop at about 337 K to 5.04 (at 333 K) in a cooling run. The ε′ in heating and cooling runs enclose a thermal hysteresis loop with a temperature window of about 3 K, *i.e.*, a thermal-induced dielectric bistability, which is similar to magnetic hysteresis loops in magnets and electric hysteresis loops in ferroelectrics. Simultaneously, the $\chi_M T$ value appears to decrease at about 338 K in the heating run and to increase at about 335 K in the cooling run, which resembles the "reverse spin transition" observed in a cobalt compound and an azido-bridged coordination framework.[21,60] This thermal hysteresis of $\chi_M T$ forms a magnetic bistability. Compared with the γ ↔ δ transition, the ordering and displacement of organic cations as well as the change of the inorganic layers between the β ↔ γ transition contribute to the change of ε′, resulting in a much larger dielectric change (Δε′ = 0.34) than that (Δε′ = 0.02) during the γ ↔ δ transition. Meanwhile, the noticeable tilting of $MnCl_6$ octahedra as well as the stagger movement of the inorganic layers make major contributions to the observed bistability of $\chi_M T$.

For the α ↔ β transition, as illustrated in Fig. 7(a), ε′ increases slowly from 4.20 (115 K, 1000 kHz) to 4.22 (180 K), then suffers a step-like increase at about 184 K until 4.54 (188 K) in the heating run, and reversely drops at about 134 K to 4.23 (at 120 K) in the cooling run, enclosing a notable thermal hysteresis loop with a large window of about 50 K. Based on the structural analyses, it can be concluded that the ordering of the organic cations, the large displacement of the organic cations and the drastic tilting of the $MnCl_6$ octahedra, jointly contribute to the remarkable dielectric bistability during the α ↔ β transition. Correspondingly, the "reverse spin transition" of $\chi_M T$ appears around 184 to 134 K in the heating-cooling circle, forming a magnetic bistability with a

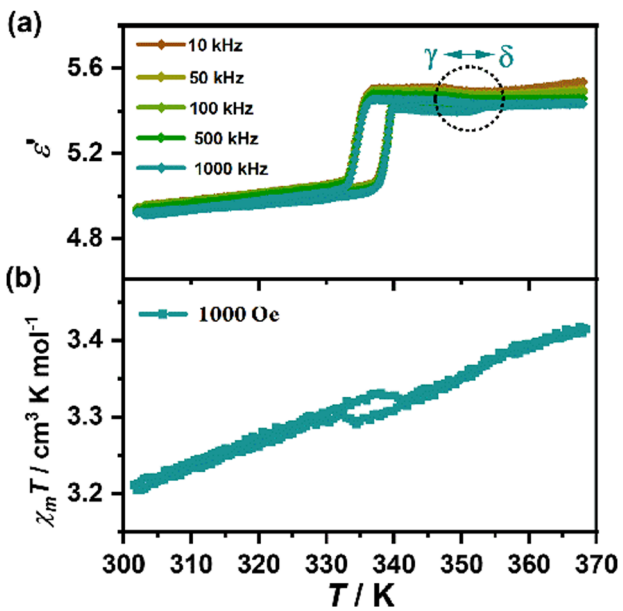

Fig. 6 Dielectric constants in various frequencies (a) and the temperature-dependence of magnetic susceptibility under 1000 Oe (b) during β ↔ γ ↔ δ in a heating–cooling circle.

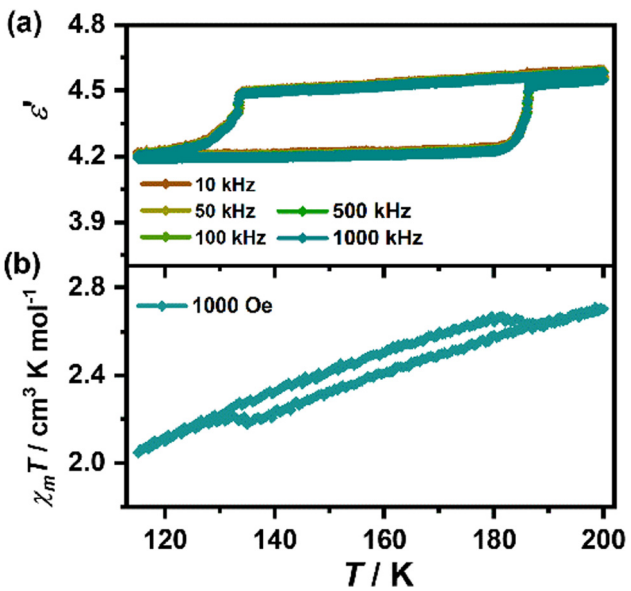

Fig. 7 Dielectric constants in various frequencies (a) and the temperature-dependence of magnetic susceptibility under 1000 Oe (b) during the α ↔ β transition in a heating–cooling circle.

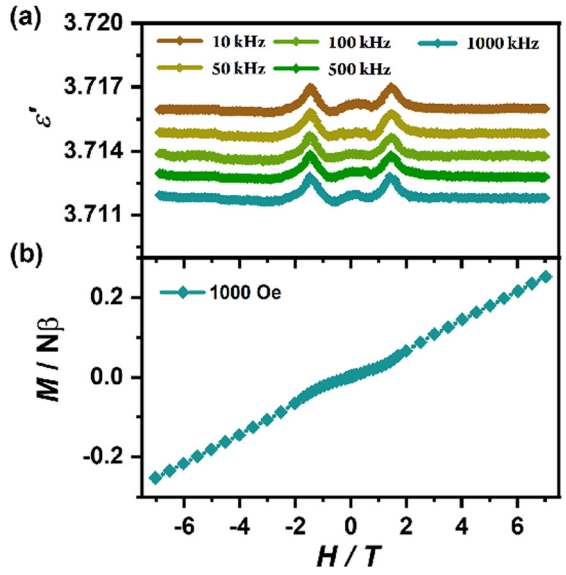

Fig. 8 Dielectric constant in various frequencies along the *c* axis (a) and magnetization for the polycrystalline sample of **1** (b) as a function of the scanning magnetic field at 3 K.

window of 50 K, which is mainly ascribed to the tilting of the $MnCl_6$ octahedra accompanied with a noticeable staggering movement of the inorganic layers.

Magnetodielectric coupling effect

For the spin-canted antiferromagnets, spin-flop transition is a unique field-induced spin-reorientation behavior in their long-range magnetic ordering states, and such spin-reorientation in layered perovskites may induce a coupling effect between dielectric and magnetic properties.[48] To probe the possible magnetodielectric coupling effect for **1**, we measured the dielectric constant as a function of the scanning magnetic field at 3 K on a single crystal applying both an electric and magnetic field along its *c* axis (*i.e.*, perpendicular to the magnetic inorganic layers). As shown in Fig. 8(a), a pair of dielectric anomaly peaks appear at about ±1.4 T (H_{sf}), corresponding to the occurrence of the spin-flop transition (Fig. 8(b)) and indicating an intrinsic magnetodielectric coupling effect. According to the structural analyses, the strong hydrogen bonds act as a medium between organic and inorganic components, mediating the dielectric and magnetic properties to achieve the coupling effect. By defining the magnetodielectric ratio as MD = $[\varepsilon'(H) - \varepsilon'(0)]/\varepsilon'(0) \times 100\%$, we can obtain a maximum MD of about 0.03% at H_{sf}. The MD is comparable with those of $((CH_3)_2NH_2)[Cu(HCOO)_3]$ (−0.02% at 3 T, −0.03% at 5 T, −0.06% at 7 T),[61] $((CH_3)_2NH_2)[Fe(HCOO)_3]$ (−0.06% at 5 T)[35] and $Co(C_{16}H_{15}N_5O_2)$ (0.038% at 5 T).[62] Compared with its analogue $(C_6H_5CH_2CH_2NH_3)_2[MnCl_4]$ showing a maximum MD of 0.34% at ±3.4 T,[48] **1** reveals a smaller maximum MD at a lower magnetic field (±1.4 T). The lower MD in **1** could be mainly ascribed to the relative rigid lattice induced by the stagger arrangement and the drastic tilting of the inorganic layers, as well as the weaker interactions between two neighboring layers along the *c* axis separated by the longer $C_6H_5(CH_2)_4NH_3^+$ organic cations. In detail, the minimum distance of Mn···Mn atoms between two neighboring layers of **1** is 22.892 Å (120 K), which is apparently larger than that of $(C_6H_5CH_2CH_2NH_3)_2[MnCl_4]$ (19.893 Å at 120 K).[48] In addition, certain damage and cracking of the high-quality crystal occurred during the drastic structural phase transition from the β to α phase, and may cause an underestimation of MD for **1**. It should be noted that, compared with the H_{sf} (about ±3.4 T) of $(C_6H_5CH_2CH_2NH_3)_2[MnCl_4]$, the H_{sf} (±1.4 T) of **1** giving the maximum MD indicates a lower manipulated magnetic field, which should benefit from the stagger arrangement and greater distance of the neighboring inorganic layers in **1**.

Conclusions

In summary, large single-crystal samples of a new organic–inorganic layered hybrid perovskite, *i.e.*, **1**, have been prepared and comprehensively characterized. The flexible character of the organic cations endows **1** with three-step structural phase transitions at 184/134 K, 338/335 K, and 354/352 K in heating/cooling runs, respectively, with space group changes of $P2_1/a$ (α) ↔ $P2_1/a$ (β) ↔ *Bmmm* (γ) ↔ $P4/mmm$ (δ). During the γ ↔ β and β ↔ α transitions, the gradual ordering and displacement of the organic cations, tilting of the $MnCl_6$ octahedra, and stagger movement of the inorganic layers in **1** jointly generate dielectric and magnetic dual-bistabilities. Moreover, the strong intermolecular interactions between the organic and inorganic components endow **1** with a rarely observed magneto-dielectric coupling effect with a maximum MD ratio of 0.03% accompanying the magnetic-field-induced spin-flop transition at a relatively low magnetic field (±1.4 T) at 3 K. Considering the diverse and controllable layered perovskites, these findings are helpful for further understanding and developing the mechanisms of the magnetoelectric effect as well as providing a new route for the rational design of multi-bistable and magnetodielectric molecule-based materials.

Conflicts of interest

There are no conflicts to declare.

Acknowledgements

This work was financially supported by the National Natural Science Foundation of China (21901227, 22071273, and 21821003), the Science and Technology Planning Project of Yunnan Province (202001AU070083), the Science Foundation from Education Department of Yunnan Province (2019J0065), and the Local Innovative and Research Teams Project of Guangdong Pearl River Talents Program (2017BT01C161).

Notes and references

1 O. Sato, *Nat. Chem.*, 2016, **8**, 644–656.

2 T. Mahfoud, G. Molnár, S. Bonhommeau, S. Cobo, L. Salmon, P. Demont, H. Tokoro, S.-I. Ohkoshi, K. Boukheddaden and A. Bousseksou, *J. Am. Chem. Soc.*, 2009, **131**, 15049–15054.
3 N. Hoshino, F. Iijima, G. N. Newton, N. Yoshida, T. Shiga, H. Nojiri, A. Nakao, R. Kumai, Y. Murakami and H. Oshio, *Nat. Chem.*, 2012, **4**, 921–926.
4 Y. Zhang, H.-Y. Ye, H.-L. Cai, D.-W. Fu, Q. Ye, W. Zhang, Q. Zhou, J. Wang, G.-L. Yuan and R.-G. Xiong, *Adv. Mater.*, 2014, **26**, 4515–4520.
5 S.-N. Du, D. Su, Z.-Y. Ruan, Y.-Q. Zhou, W. Deng, W.-X. Zhang, Y. Sun, J.-L. Liu and M.-L. Tong, *Angew. Chem., Int. Ed.*, 2022, **61**, e202204700.
6 N.-T. Yao, L. Zhao, C. Yi, Q. Liu, Y.-M. Li, Y.-S. Meng, H. Oshio and T. Liu, *Angew. Chem., Int. Ed.*, 2022, **61**, e202115367.
7 R. Podgajny, S. Chorazy, W. Nitek, M. Rams, A. M. Majcher, B. Marszalek, J. Zukrowski, C. Kapusta and B. Sieklucka, *Angew. Chem., Int. Ed.*, 2013, **52**, 896–900.
8 A. Ueda, S. Yamada, T. Isono, H. Kamo, A. Nakao, R. Kumai, H. Nakao, Y. Murakami, K. Yamamoto, Y. Nishio and H. Mori, *J. Am. Chem. Soc.*, 2014, **136**, 12184–12192.
9 C. Chen, W.-Y. Zhang, H.-Y. Ye, Q. Ye and D.-W. Fu, *J. Mater. Chem. C*, 2016, **4**, 9009–9020.
10 J.-P. Zhao, J. Xu, S.-D. Han, Q.-L. Wang and X.-H. Bu, *Adv. Mater.*, 2017, **29**, 1606966.
11 R.-G. Xiong, S.-Q. Lu, Z.-X. Zhang, H. Cheng, P.-F. Li and W.-Q. Liao, *Angew. Chem., Int. Ed.*, 2020, **59**, 9574–9578.
12 W.-J. Xu, Z.-Y. Du, W.-X. Zhang and X.-M. Chen, *CrystEngComm*, 2016, **18**, 7915–7928.
13 H. Cui, Z. Wang, K. Takahashi, Y. Okano, H. Kobayashi and A. Kobayashi, *J. Am. Chem. Soc.*, 2006, **128**, 15074–15075.
14 P. Jain, V. Ramachandran, R.-J. Clark, H.-D. Zhou, B.-H. Toby, N.-S. Dalal, H.-W. Kroto and A.-K. Cheetham, *J. Am. Chem. Soc.*, 2009, **131**, 13625–13627.
15 D.-W. Fu, W. Zhang, H.-L. Cai, Y. Zhang, J.-Z. Ge, R.-G. Xiong, S. D. Huang and T. Nakamura, *Angew. Chem., Int. Ed.*, 2011, **50**, 11947–11951.
16 G.-C. Xu, W. Zhang, X.-M. Ma, Y.-H. Chen, L. Zhang, H.-L. Cai, Z.-M. Wang, R.-G. Xiong and S. Gao, *J. Am. Chem. Soc.*, 2011, **133**, 14948–14951.
17 X.-H. Zhao, X.-C. Huang, S.-L. Zhang, D. Shao, H.-Y. Wei and X.-Y. Wang, *J. Am. Chem. Soc.*, 2013, **135**, 16006–16009.
18 P.-P. Shi, Q. Ye, Q. Li, H.-T. Wang, D.-W. Fu, Y. Zhang and R.-G. Xiong, *Chem. Mater.*, 2014, **26**, 6042–6049.
19 Y.-P. Gong, X.-X. Chen, G.-Z. Huang, W.-X. Zhang and X.-M. Chen, *J. Mater. Chem. C*, 2022, **10**, 5482–5488.
20 W.-J. Xu, C.-T. He, C.-M. Ji, S.-L. Chen, R.-K. Huang, R.-B. Lin, W. Xue, J.-H. Luo, W.-X. Zhang and X.-M. Chen, *Adv. Mater.*, 2016, **28**, 5886–5890.
21 Z.-H. Sun, X.-F. Yi, K.-W. Tao, C.-M. Ji, X.-T. Liu, L.-N. Li, S.-G. Han, A.-M. Zheng, M.-C. Hong and J.-H. Luo, *Angew. Chem., Int. Ed.*, 2018, **130**, 9981–9985.
22 N. A. Spaldin and R. Ramesh, *Nat. Mater.*, 2019, **18**, 203–212.
23 X.-L. Liu, D. Li, H.-X. Zhao, X.-W. Dong, L.-S. Long and L.-S. Zheng, *Adv. Mater.*, 2021, **33**, e2004542.
24 J. Long, M. S. Ivanov, V. A. Khomchenko, E. Mamontova, J. M. Thibaud, J. Rouquette, M. Beaudhuin, D. Granier, R. A. S. Ferreira, L. D. Carlos, B. Donnadieu, M. S. C. Henriques, J. A. Paixao, Y. Guari and J. Larionova, *Science*, 2020, **367**, 671–676.
25 R. Gupta and R. K. Kotnala, *J. Mater. Sci.*, 2022, **57**, 12710–12737.
26 T. Lottermoser, T. Lonkai, U. Amann, D. Hohlwein, J. Ihringer and M. Fiebig, *Nature*, 2004, **430**, 541–544.
27 X. Wang, Y.-H. Chai, L. Zhou, H.-B. Cao, C. D. Cruz, J.-Y. Yang, J.-H. Dai, Y.-Y. Yin, Z. Yuan, S.-J. Zhang, R.-Z. Yu, M. Azuma, Y. Shimakawa, H.-M. Zhang, S. Dong, Y. Sun, C. Jin and Y.-W. Long, *Phys. Rev. Lett.*, 2015, **115**, 087601.
28 J. Zhang, Y. Zhou, F. Wang, X. Shen, J. Wang and X. Lu, *Phys. Rev. Lett.*, 2022, **129**, 117603.
29 T. Goto, T. Kimura, G. Lawes, A. P. Ramirez and Y. Tokura, *Phys. Rev. Lett.*, 2004, **92**, 257201.
30 T. Kimura, T. Goto, H. Shintani, K. Ishizaka, T. Arima and Y. Tokura, *Nature*, 2003, **426**, 55–58.
31 N. Hur, S. Park, P. A. Sharma, J. S. Ahn, S. Guha and S. W. Cheong, *Nature*, 2004, **429**, 392–395.
32 M. A. Subramanian, T. He, J. Z. Chen, N. S. Rogado, T. G. Calvarese and A. W. Sleight, *Adv. Mater.*, 2006, **18**, 1737–1739.
33 Y. Kitagawa, Y. Hiraoka, T. Honda, T. Ishikura, H. Nakamura and T. Kimura, *Nat. Mater.*, 2010, **9**, 797–802.
34 W. Wang, L.-Q. Yan, J.-Z. Cong, Y.-L. Zhao, F. Wang, S.-P. Shen, T. Zou, D. Zhang, S.-G. Wang, X.-F. Han and Y. Sun, *Sci. Rep.*, 2013, **3**, 2024.
35 Y. Tian, A. Stroppa, Y. Chai, L. Yan, S. Wang, P. Barone, S. Picozzi and Y. Sun, *Sci. Rep.*, 2014, **4**, 6062.
36 Y. Tian, S. Shen, J. Cong, L. Yan, S. Wang and Y. Sun, *J. Am. Chem. Soc.*, 2016, **138**, 782–785.
37 L. C. Gomez-Aguirre, B. Pato-Doldan, J. Mira, S. Castro-Garcia, M. A. Senaris-Rodriguez, M. Sanchez-Andujar, J. Singleton and V. S. Zapf, *J. Am. Chem. Soc.*, 2016, **138**, 1122–1125.
38 J. Guo, L. Chen, D. Li, H. Zhao, X. Dong, L. Long, R. Huang and L. Zheng, *Appl. Phys. Lett.*, 2017, **110**, 192902.
39 Y.-X. Wang, Y. Ma, Y. Chai, W. Shi, Y. Sun and P. Cheng, *J. Am. Chem. Soc.*, 2018, **140**, 7795–7798.
40 Y. Yang, J. Ji, J. Feng, S. Chen, L. Bellaiche and H. Xiang, *J. Am. Chem. Soc.*, 2022, **144**, 14907–14914.
41 Y. Ma, J. Cong and Y. Sun, *J. Phys.: Condens. Matter*, 2019, **31**, 205701.
42 X. Liu, B. Wang, X. Huang, X. Dong, Y. Ren, H. Zhao, L. Long and L. Zheng, *J. Am. Chem. Soc.*, 2021, **143**, 5779–5785.
43 D. Li, X.-M. Zhao, H.-X. Zhao, X.-W. Dong, L.-S. Long and L.-S. Zheng, *Adv. Mater.*, 2018, **30**, 1803716.
44 T. Basu, C. Bloyet, F. Beaubras, V. Caignaert, O. Perez, J. M. Rueff, A. Pautrat, B. Raveau, J. F. Lohier, P. A. Jaffrès, H. Couthon, G. Rogez, G. Taupier and H. Dorkenoo, *Adv. Funct. Mater.*, 2019, **29**, 1901878.
45 D. Li, X. Wang, H.-X. Zhao, Y.-P. Ren, G.-L. Zhuang, L.-S. Long and L.-S. Zheng, *Angew. Chem., Int. Ed.*, 2020, **59**, 14409–14413.
46 Y. Ai, R. Sun, Y.-L. Zeng, J.-C. Liu, Y.-Y. Tang, B.-W. Wang, Z.-M. Wang, S. Gao and R.-G. Xiong, *Chem. Sci.*, 2021, **12**, 9742–9747.

47 L.-H. Chen, J.-B. Guo, X. Wang, X.-W. Dong, H.-X. Zhao, L.-S. Long and L.-S. Zheng, *Adv. Mater.*, 2017, **29**, 1702512.
48 B. Huang, J.-Y. Zhang, R.-K. Huang, M.-K. Chen, W. Xue, W.-X. Zhang, M.-H. Zeng and X.-M. Chen, *Chem. Sci.*, 2018, **9**, 7413–7418.
49 B. Huang, B.-Y. Wang, Z.-Y. Du, W. Xue, W.-J. Xu, Y.-J. Su, W.-X. Zhang, M.-H. Zeng and X.-M. Chen, *J. Mater. Chem. C*, 2016, **4**, 8704–8710.
50 S. H. Park, I. H. Oh, S. Park, Y. Park, J. H. Kim and Y. D. Huh, *Dalton Trans.*, 2012, **41**, 1237–1242.
51 Y. Nakayama, S. Nishihara, K. Inoue, T. Suzuki and M. Kurmoo, *Angew. Chem., Int. Ed.*, 2017, **56**, 9367–9370.
52 Y. Ai, R. Sun, W.-Q. Liao, X.-J. Song, Y.-Y. Tang, B.-W. Wang, Z.-M. Wang, S. Gao and R.-G. Xiong, *Angew. Chem., Int. Ed.*, 2022, **61**, e202206034.
53 Y. H. Kim and N. Hur, *J. Korean Phys. Soc.*, 2020, **77**, 1026–1030.
54 Q.-R. Kong, D. Li, X.-L. Liu, H.-X. Zhao, Y.-P. Ren, L.-S. Long and L.-S. Zheng, *Inorg. Chem.*, 2021, **60**, 3565–3571.
55 Y. H. Kim and N. Hur, *J. Appl. Phys.*, 2021, **129**, 224101.
56 T. Hu and E. Kan, *Wiley Interdiscip. Rev.: Comput. Mol. Sci.*, 2019, e1409.
57 B. Sun, X.-F. Liu, X.-Y. Li, Y. Cao, Z. Yan, L. Fu, N. Tang, Q. Wang, X. Shao, D. Yang and H.-L. Zhang, *Angew. Chem., Int. Ed.*, 2020, **59**, 203–208.
58 L. Septiany, D. Tulip, M. Chislov, J. Baas and G. R. Blake, *Inorg. Chem.*, 2021, **60**, 15151–15158.
59 A. T.-S. A. Daoud, R. Perret and B. Chaillot, *Rev. Roum. Chim.*, 1977, **22**, 857.
60 S. Hayami, Y. Shigeyoshi, M. Akita, K. Inoue, K. Kato, K. Osaka, M. Takata, R. Kawajiri, T. Mitani and Y. Maeda, *Angew. Chem., Int. Ed.*, 2005, **44**, 4899–4903.
61 Z. Wang, P. Jain, K.-Y. Choi, J. van Tol, A. K. Cheetham, H. W. Kroto, H.-J. Koo, H. Zhou, J. Hwang, E. S. Choi, M.-H. Whangbo and N. S. Dalal, *Phys. Rev. B: Condens. Matter Mater. Phys.*, 2013, **87**, 224406.
62 T. Basu, A. Jesche, B. Bredenkötter, M. Grzywa, D. Denysenko, D. Volkmer, A. Loidl and S. Krohns, *Mater. Horiz.*, 2017, **4**, 1178–1184.